RESEARCH ARTICLE

Ablation Study of a Dynamic Model for a 3D-Printed Pneumatic Soft Robotic Arm

CARLO ALESSI[1,2], **EGIDIO FALOTICO**[1,2], **(Member, IEEE),**
AND ALESSANDRO LUCANTONIO[3]

[1]The BioRobotics Institute, Scuola Superiore Sant'Anna, 56025 Pontedera, Italy
[2]Department of Excellence in Robotics and AI, Scuola Superiore Sant'Anna, 56127 Pisa, Italy
[3]Department of Mechanical and Production Engineering, Aarhus University, 8000 Aarhus, Denmark

Corresponding author: Carlo Alessi (carlo.alessi@santannapisa.it)

ABSTRACT Ongoing advancements in the design and fabrication of soft robots are creating new challenges in modeling and control. This paper presents a dynamic Cosserat rod model for a single-section 3D-printed pneumatic soft robotic arm capable of combined stretching and bending. The model captures the manufacturing variability of the actuators by tuning the pressure-strain relation for each actuator. Moreover, it includes a simple model of the pneumatic actuation system that incorporates the transient response of proportional pressure-controlled electronic valves. The model was validated experimentally for several quasi-static and dynamic motion patterns with actuation frequencies ranging from 0.2 Hz to 20 Hz. The model reproduced the quasi-static experiments with an average tip error of 4.83% of the arm length. In dynamic conditions, the average tip error was 4.33% for stretching and bending motions, 5.64% for five motor babbling experiments, and 22.53% for three challenging sinusoidal patterns. An ablation study of the model components found that the most influential factors for the average accuracy were gravity and strain gains, followed by damping and pressure transient. This work could assist researchers in focusing on the most significant aspects for closing the real-to-sim gap when modeling pneumatic soft robotic arms.

INDEX TERMS Soft robot model, Cosserat rod, pneumatic actuators.

I. INTRODUCTION

Continuum and soft robotic arms manufactured using compliant materials can bend, twist, stretch, and shear while safely interacting with unstructured environments [1]. Recent progress in design and manufacturing technologies (e.g., 3D-printing) enabled the rapid prototyping of complex soft robotic systems [2]. However, the elastic deformations of the soft materials cause extreme hyper-redundancy. Soft materials also exhibit nonlinear behaviors like hysteresis, viscoelasticity, and stress softening. As a result, traditional modeling and control methods that assume rigid links are not directly applicable [3]. These challenges led to the development of alternative modeling [4] and control strategies [5].

The associate editor coordinating the review of this manuscript and approving it for publication was Yizhang Jiang.

Data-driven models for soft robots do not require physical considerations but rely on experimental or synthetic data typically collected performing pseudo-random motions (i.e., motor babbling). Then, artificial neural networks trained with machine learning algorithms map actuation to task space [6]. This platform-independent approach effectively derived computationally efficient static [7] and dynamic models [8], [9]. However, the limitations might be the need for representative data, extensive optimization time, and overfitting.

Discrete material models discretize continuous bodies a priori. For example, pseudo-rigid models represent them with a chain of rigid links connected by joints. While these provide satisfactory results for hyper-redundant arms [10], they poorly approximate elastic structures. In addition, lumped-mass models employ an array of masses, springs, and dampers [11]. This modularity can model complex phenomena but could require intensive system identification.

Geometrical models utilize geometrical assumptions on the deformed shape of the soft body. For instance, functional models describe the deformations using polynomials [12]. In addition, piecewise constant curvature (PCC) models discretize continuous bodies in circular arcs with constant curvature [13]. Most continuum arms present actuators parallel to the centerline producing constant-curvature deformations, making PCC viable for uniform and lightweight robots [14]. However, the suitability of these approximations could degrade when the robot is subject to significant external forces and unpredictable interaction with the environment.

Continuum mechanics models characterize soft robots with continuous configuration spaces and define deformations in physical terms. These enable the simulation of the interaction with the environment and the study of the mechanics of the robotic platforms. The classical three-dimensional (3D) finite element method (FEM) accurately represents complex geometries to the extent of high computational costs and involved mathematical formulations [15]. Since such models would be difficult to interface with controllers in real-time applications, their use is usually limited to designing and simulating soft robotic components [16] or benchmarking other methods. Nonetheless, ad-hoc FEM techniques targeting soft robotics are making 3D mechanical models more appealing [17], [18]. Other viable approaches employ reduced-order models like Cosseat rods [19], which effectively describe slender bodies undergoing large deflections in all deformation modes, striking a good balance between the computational efficiency of data-driven models and the accuracy of 3D mechanical models.

Cosserat theory was applied to compute in real-time the kinematics of tendon-actuated robots subject to external loads, modeling the tendon actuation as a single point moment applied to the backbone where each tendon is attached [20]. This approach was extended by including the attachment point force and the distributed wrench that tendons apply along the backbone [21]. The authors modeled the statics and dynamics of robots with general tendon routing paths by coupling the classical Cosserat rod and Cosserat string models. They validated the model on static experiments performing planar and 3D movements with various tendon routings. In another work, [22] presented a geometrically exact static Cosserat rod model of a tendon-driven soft robotic arm made of silicone inspired by the octopus arm. They modeled the cable tension as a pure tension element neglecting friction between the cable and the silicone. After a theoretical validation of the algebraic correctness of the equations using a FEM model, the Cosserat model was validated experimentally in static conditions by actuating one cable resulting in a planar motion. The approach was later expanded in [23] to investigate the dynamic interaction with a dense medium and the coupled tendon condition, addressing all the hydrodynamic forces like gravity, buoyancy, drag, added mass, and cable load. The dynamic experiments validated how the prototype and the model performed characteristic octopus movements. An ablation study of the model components suggested that minimal internal viscosity guaranteed solution stability and minimized computational costs and that the environment drag load most significantly contributed to the arm dynamics.

Recently, it was introduced a dynamic Cosserat model for concentric tube robots [24]. The model described the coupled inertial dynamics of a collection of pre-curved concentric tubes considering linear and rotational tube inertia, material damping, Coulomb and viscous friction, and the inertia of a rigid body held at the end-effector. Experiments validated the snapping phenomenon and a tissue grasping task.

For electric soft robots, [25] presented a dynamic Cosserat model for a hydrogel-based planar cantilever arm composed of a 3D-printed elastic backbone and orthogonal plates supporting cubical soft voxel actuators (SVA), which bend the centerline when a voltage is applied. They identified the map between an input voltage and the tensile force for a single voxel, while vibration tests estimated elastic modulus and damping coefficient. The experimental dynamic validation consisted of planar movements obtained by actuating subsets of SVAs with square signals.

In the context of pneumatic soft robotic arms, Trivedi et al. [26] proposed a dynamic model for the OctArm V continuum arm based on a geometrically exact Cosserat rod and a fiber-reinforced model of the air muscle actuators. The model was experimentally validated statically for planar movements with vertical and horizontal base orientation. Recently, Uppalapati et al. [27] presented a dynamic Cosserat rod model to capture the deformations of a soft robotic arm composed of two asymmetric pneumatic actuators, which respectively bend and rotate. They optimized the flexural and torsional rigidity and the spontaneous curvature and torsion for a set of quasi-static arm positions. The experimental validation of the model assessed its ability to reproduce the workspace with an end-point load. Gilbert and Godage [28] used the classical Cosserat rod approach to model a variable-length pneumatic soft robotic arm. After optimizing the cross-sectional area and a parameter relating stiffness and damping in the constitutive law, the model was validated on dynamic bending movements obtained by pressurizing the actuators with alternating square pulses. Eugster et al. [29] described the kinematics of a three-chamber soft pneumatic actuator that can stretch and bend. They derived a Cosserat rod theory with a nonlinear pressure-dependent constitutive law using the principle of virtual work and modeled the actuator with strain energy functions. They accounted for manufacturing imperfections by scaling the relations of extensional and bending stiffness and by repositioning the chambers on the cross-section. A static validation consisted of stretching and bending motions in vertical and horizontal setups.

Previous Cosserat rod models for pneumatic soft robotic arms considered instantaneous pressure changes ignoring the transient behavior of the pneumatic actuation system. In practice, the contribution of the pressure transient can be

significant to model accuracy. Detailed dynamic descriptions of pneumatic systems were included in models of soft robotic arms based on lumped mass [30], [31], black-box system identification [32] and PCC [33]. We provide a functional approximation of the pneumatic system dynamics and integrate it into a Cosserat rod model of a pneumatic soft robotic arm.

This paper presents a dynamic Cosserat rod model of a 3D-printed pneumatic soft robotic arm capable of stretching and bending. We model pressure-induced strains as spontaneous stretching and bending. The model captures the manufacturing irregularities of the pneumatic chambers using strain gains that tune the pressure-strain relation for each actuator. Moreover, we include a practical analytical approximation of the pneumatic actuation system that captures the transient response of proportional pressure-controlled electronic valves. We perform an extensive experimental validation in quasi-static and dynamic conditions for a wide range of motion patterns: (i) stretching, (ii) bending with one chamber, (iii) bending with two chambers, (iv) quasi-static workspace, (v) five motor babbling experiments at various actuation frequencies, and (vi) three sinusoidal motions at different frequencies. In addition, we conduct an ablation study to evaluate how different model components contribute to the accuracy. Specifically, the four analyzed model features are gravity, damping, actuator strain gains, and pressure transient. As soft robots are frequently subject to perturbations from the interaction with the environment, we assess the impact of gravity as an instance of distributed external force. Moreover, the ablation of the strain gains of the actuators measures the effect of actuator asymmetries, which could arise from manufacturing variability or material degradation. Finally, we evaluate the dynamic behavior of the soft material and the pneumatic actuation system by ablating the damping mechanism and the pressure transient. We compare the performance of the comprehensive model against ablated model variations on eight dynamic motion patterns. This study contributes to a better understanding of how physical phenomena affect models of pneumatic soft robotic arms. Therefore, this work could form a guideline for directing the focus of researchers intending to design, manufacture, model, and control pneumatic soft robotic arms.

Section II describes the soft robotic platform. Section III describes the Cosserat rod model. Section IV reports the experimental materials and protocols. Section V discusses the performance results of the experimental validation, while section VI studies the ablation of the main model components. Finally, section VII summarizes the main findings and concludes with an insight into future works.

II. ROBOTIC PLATFORM: THE AM I-SUPPORT

The AM I-Support is a 3D-printed soft robotic arm with three elliptical pneumatic chambers that generate large deformations by combining stretching and bending [34]. As shown in Fig. 1, two terminal plates (top and bottom) confine the modules, and six rings distributed along the body
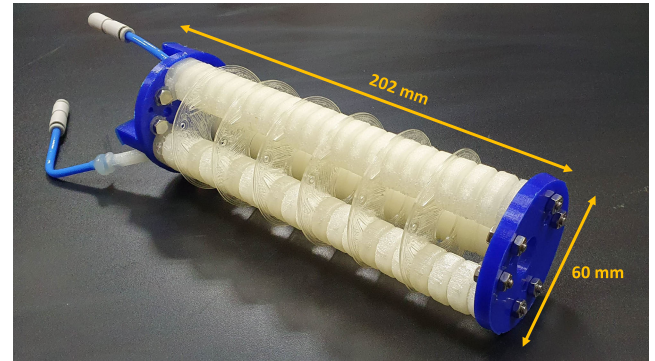

FIGURE 1. One module of the AM I-Support robotic arm.

constrain the chambers, while nuts and bolts assemble the parts.

The soft robotic arm has a circular cross-section of a radius of 30 mm, an overall length of ~202 mm, and ~183 g overall weight. The pneumatic chambers are ~180 mm long, while the top and bottom terminals are ~20 mm and ~5 mm long, respectively. The actuators are distributed axially, at a radial distance of $\delta = 20$ mm from the cross-section centroid, and equally spaced by $\theta = 120°$ around the center (see Fig. 2). In addition, both terminals have seats to insert the chambers. The wall thickness of the chambers is $t_w = 1.4$ mm.

The pneumatic chambers and disks of the soft robotic arm were fabricated using the soft material thermoplastic polyurethane with 80 Shore A hardness (TPU 80 A LF, BASF). The terminals were printed using TPU 95A, Ultimaker. The specifics on actuator design and manufacturing process (e.g., 3D printing parameters) are reported in [34].

Note that the three chambers share the same design but could exhibit different stretching when subject to equal pressure due to manufacturing irregularities. The proposed model captures this feature. Moreover, it could describe other soft robotic arms employing linear pneumatic actuators having similar geometries and different materials [35].

III. MATHEMATICAL MODEL

We model the soft robotic arm as a Cosserat rod with a constant cross-section (see Fig. 2) and homogeneous material properties, leveraging and extending the Cosserat theory in [36] and [37]. A rod is described by a center-line $\boldsymbol{r}(s,t) \in \mathbb{R}^3$ and a local oriented reference frame $\boldsymbol{Q}(s,t) \in SO(3)$, defined by the orthonormal triad of vectors $\boldsymbol{Q} = \{\boldsymbol{d}_1, \boldsymbol{d}_2, \boldsymbol{d}_3\}$. Here, $t \in \mathbb{R}^+$ is time, $s \in [0, L]$ is the center-line arc-length coordinate in its current configuration, while the reference quantity is denoted by $\hat{s}$. Vectors $\boldsymbol{x}$ are expressed either in the global reference frame or in the local reference frame

$$\text{global:} \quad \boldsymbol{x} = \bar{x}_1 \boldsymbol{i} + \bar{x}_2 \boldsymbol{j} + \bar{x}_3 \boldsymbol{k} \qquad (1)$$

$$\text{local:} \quad \boldsymbol{x}_{\mathcal{L}} = x_1 \boldsymbol{d}_1 + x_2 \boldsymbol{d}_2 + x_3 \boldsymbol{d}_3, \qquad (2)$$

where $\{\boldsymbol{i}, \boldsymbol{j}, \boldsymbol{k}\}$ is the canonical basis and $\{\boldsymbol{d}_1, \boldsymbol{d}_2, \boldsymbol{d}_3\}$ is the body-convected director basis. The orthogonal matrix $\boldsymbol{Q}$
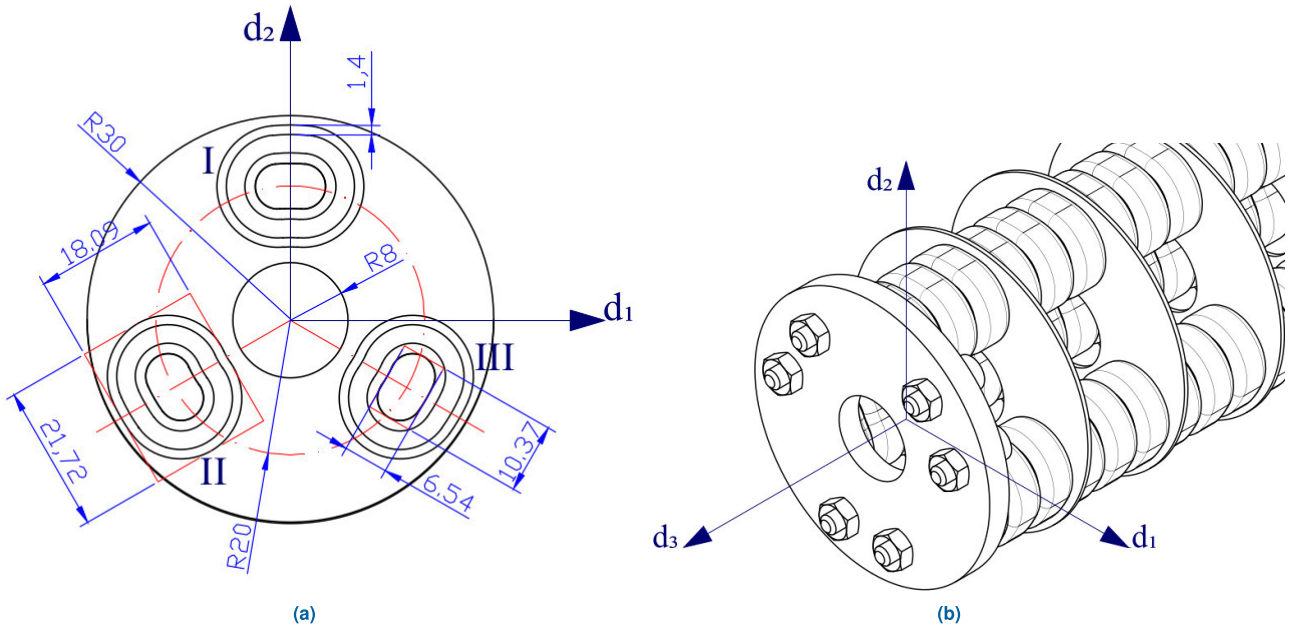
FIGURE 2. View of (a) the cross-section and (b) the free-end of the robot and model. Refer to [34] for additional information on the actuators design.

transforms vectors from one representation into another via $x_{\mathcal{L}} = Qx$, and vice versa $x = Q^{\mathsf{T}}x_{\mathcal{L}}$. The local frame describes the orientation of the rod, where (d_1, d_2) span the normal-binormal plane of the cross-section, and d_3 points along the center-line tangent ($\partial_s r = t$) when there is no shear. The deformations that the rod can undergo are expressed by the shear/stretch vector $\sigma_{\mathcal{L}}(s, t)$ and the bend/twist vector $\kappa_{\mathcal{L}}(s, t)$

$$\sigma_{\mathcal{L}} = (\sigma_1 d_1 + \sigma_2 d_2 + \sigma_3 d_3) = Q(et - d_3) \qquad (3)$$
$$\kappa_{\mathcal{L}} = (\kappa_1 d_1 + \kappa_2 d_2 + \kappa_3 d_3). \qquad (4)$$

In particular, (σ_1, σ_2) are the shear strains along (d_1, d_2), and σ_3 is the axial strain along d_3. Likewise, (κ_1, κ_2) characterize bending about (d_1, d_2), and κ_3 is the torsion about d_3. The scalar $e(\hat{s}, t) = ds/d\hat{s}$ is the stretching ratio.

A. GOVERNING EQUATIONS
The rod dynamics is governed by the following set of non linear differential equations:

$$\partial_t r = v \qquad (5)$$
$$\partial_t d_j = \left(Q^{\mathsf{T}}\omega_{\mathcal{L}}\right) \times d_j, \qquad j = 1, 2, 3 \qquad (6)$$
$$\partial_t(\rho A v) = \partial_s \left(Q^{\mathsf{T}}\tilde{n}_{\mathcal{L}}\right) + f \qquad (7)$$
$$\partial_t(\rho I \omega_{\mathcal{L}}) = \partial_s \tilde{m}_{\mathcal{L}} + \kappa_{\mathcal{L}} \times \tilde{m}_{\mathcal{L}}$$
$$+ Q\partial_s r \times \tilde{n}_{\mathcal{L}} + (\rho I \omega_{\mathcal{L}}) \times \omega_{\mathcal{L}}$$
$$+ c_{\mathcal{L}}, \qquad (8)$$

where v is the linear velocity, $\omega_{\mathcal{L}}$ is the angular velocity, ρ is the constant material density, A is the cross-sectional area, I is the second area moment of inertia, f is the external force, and $c_{\mathcal{L}}$ is the external couple. We define $\tilde{n}_{\mathcal{L}} = n_{\mathcal{L}} - n_p$ and

$\tilde{m}_{\mathcal{L}} = m_{\mathcal{L}} - m_p$ as the effective internal forces and moments respectively, where n_p and m_p express the active force and moments due to actuation, while $n_{\mathcal{L}}$ and $m_{\mathcal{L}}$ are the resultant internal forces and moments. The complete kinematics and dynamics of the Cosserat rod are finally obtained by defining the constitutive laws, the initial and boundary conditions.

B. CONSTITUTIVE LAWS
The relation between effective internal forces $\tilde{n}_{\mathcal{L}}$ and internal torques $\tilde{m}_{\mathcal{L}}$ with deformations are described by the constitutive laws. The rod is assumed to be composed of a linearly elastic material, so that the constitutive laws read

$$\tilde{n}_{\mathcal{L}} = S \left(\sigma_{\mathcal{L}} - \sigma^0_{\mathcal{L}}\right) \qquad (9)$$
$$\tilde{m}_{\mathcal{L}} = B \left(\kappa_{\mathcal{L}} - \kappa^0_{\mathcal{L}}\right), \qquad (10)$$

where S is the shear/stretch stiffness matrix, B is the bend/twist stiffness matrix, while $\sigma^0_{\mathcal{L}}$ and $\kappa^0_{\mathcal{L}}$ represent spontaneous strains of the rod. For an isotropic material, the stiffness matrices read

$$S = \mathrm{diag}\,(GA, GA, EA) \qquad (11)$$
$$B = \mathrm{diag}\,(EI_1, EI_2, GI_3), \qquad (12)$$

where I_i is the second area moment of inertia about the director d_i, A is the cross-sectional area, E is the elastic modulus, and G is the shear modulus.

In addition, when the rod undergoes axial stretching the infinitesimal material elements deform accordingly. Assuming material incompressibility and that the cross-section remain circular, the related geometric quantities are

rescaled

$$A = \frac{\hat{A}}{e}, \ I = \frac{\hat{I}}{e^2}, \ B = \frac{\hat{B}}{e^2}, \ S = \frac{\hat{S}}{e}, \ \kappa_{\mathcal{L}} = \frac{\hat{\kappa}_{\mathcal{L}}}{e}. \quad (13)$$

C. PRESSURE-INDUCED STRAINS

To describe the deformations of the robot, we modelled pressure-induced strains as spontaneous stretching and bending, modifying dynamically the rest configuration of the arm encoded in $\sigma^0{}_{\mathcal{L}}$ and $\kappa^0{}_{\mathcal{L}}$. The pressurization of the pneumatic chambers produces an internal force component along the local director d_3, which is normal to the rod cross-section (see Fig. 2). The active internal force and moment due to actuation of N pneumatic chambers are

$$\boldsymbol{n}_p = \sum_{i=1}^{N} F_i \boldsymbol{d}_3 \quad (14)$$

$$\boldsymbol{m}_p = \sum_{i=1}^{N} \boldsymbol{r}_i \times F_i \boldsymbol{d}_3, \quad (15)$$

where $F_i = p_i A_i$ is the force magnitude caused by pressurizing the i-th actuator with area of the interior of the actuator's cross-section A_i and pressure p_i, while $\boldsymbol{r}_i$ is the position of the centre of the actuator with respect to the local reference frame on the cross-section

$$\boldsymbol{r}_i = \delta_i \cos \theta_i \boldsymbol{d}_1 + \delta_i \sin \theta_i \boldsymbol{d}_2, \quad (16)$$

where δ_i is the distance of the actuator centre from the centre of the cross-section, and θ_i is the angular position of the actuator with respect to the director $\boldsymbol{d}_1$. By combining equations (9)-(10) and (14)-(16), the following relations hold

$$\sigma^0_{\mathcal{L}3} = \frac{1}{EA} \boldsymbol{n}_p \cdot \boldsymbol{d}_3 \quad (17)$$

$$\kappa^0_{\mathcal{L}1} = \frac{1}{EI_1} \boldsymbol{m}_p \cdot \boldsymbol{d}_1 \quad (18)$$

$$\kappa^0_{\mathcal{L}2} = -\frac{1}{EI_2} \boldsymbol{m}_p \cdot \boldsymbol{d}_2, \quad (19)$$

where

$$\sigma^0_{\mathcal{L}3} = \frac{1}{EA} \sum_{i=1}^{N} F_i \quad (20)$$

$$\kappa^0_{\mathcal{L}1} = \frac{1}{EI_1} \sum_{i=1}^{N} F_i \delta_i \sin \theta_i \quad (21)$$

$$\kappa^0_{\mathcal{L}2} = -\frac{1}{EI_2} \sum_{i=1}^{N} F_i \delta_i \cos \theta_i. \quad (22)$$

Observe that the axial strain $\sigma^0_{\mathcal{L}3}$ is given by averaging the axial strains ϵ_i of the actuators, i.e.

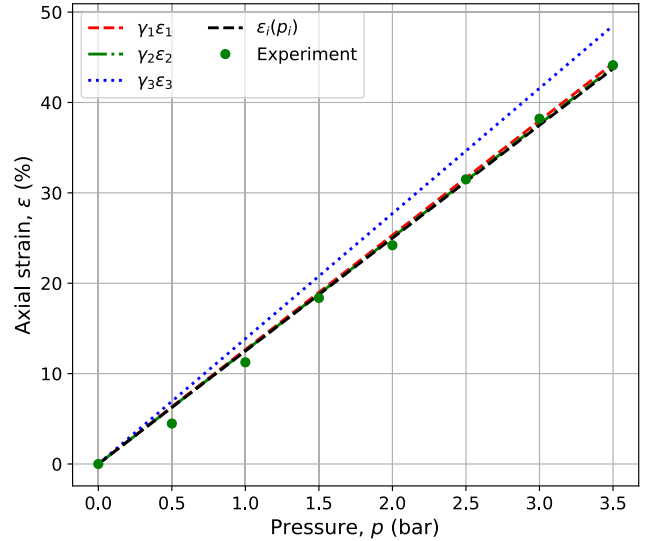$$\frac{1}{EA} \sum_{i=1}^{N} F_i = \frac{1}{N} \sum_{i=1}^{N} \epsilon_i. \quad (23)$$

FIGURE 3. Analytical pressure-strain relation $\epsilon(p)$ vs experimental stretching data. Gains $\gamma = (1.0133, 1.0035, 1.1092)$ tune the actuators axial strain.

From (23) we derive the pressure-strain relation for a single actuator

$$\epsilon_i(p_i) = N \frac{A_i}{EA} p_i. \quad (24)$$

As shown in Fig. 3, the analytical pressure-strain relation matches experimental data fairly well when E is used as a fitting parameter for a single actuator. Finally, we express the spontaneous stretching and bending deformations of the rod as a function of the strains of the actuators

$$\sigma^0_{\mathcal{L}} = \begin{pmatrix} 0 & 0 & \frac{1}{N} \sum_{i=1}^{N} \epsilon_i \end{pmatrix}^{\mathsf{T}} \quad (25)$$

$$\kappa^0_{\mathcal{L}} = \begin{pmatrix} \frac{1}{I_1} \sum_{i=1}^{N} \epsilon_i a_i \delta_i \sin \theta_i \\ -\frac{1}{I_2} \sum_{i=1}^{N} \epsilon_i a_i \delta_i \cos \theta_i \\ 0 \end{pmatrix}. \quad (26)$$

D. STRAIN GAINS

Each module of the AM I-Support robot is composed of N pneumatic chambers. These actuators exhibit different axial strains when subject to the same input pressure. This behavior emerges from several factors, including irregularities in the manufacturing process. To account for this, we scaled the collection $\boldsymbol{\epsilon} = (\epsilon_1, \ldots, \epsilon_N)^{\mathsf{T}}$ of the strains of the actuators by the strain gain matrix $\boldsymbol{\Gamma} = \text{diag}(\gamma_1, \ldots, \gamma_N)$ such that the effective strains of the actuators become

$$\boldsymbol{\epsilon} \leftarrow \boldsymbol{\Gamma}\boldsymbol{\epsilon} = \begin{pmatrix} \gamma_1 \epsilon_1 & \ldots & \gamma_N \epsilon_N \end{pmatrix}^{\mathsf{T}}. \quad (27)$$

Fig. 3 shows how $\boldsymbol{\Gamma}$ tunes the stress-strain response.

E. PNEUMATIC ACTUATION MODEL

To better describe the dynamics of the arm, we also included an approximation of the pneumatic actuation system. Rather than assuming instantaneous pressure changes, we captured
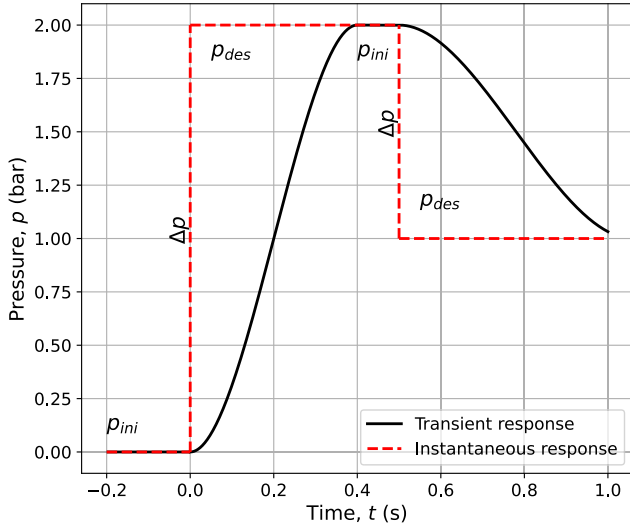
FIGURE 4. Pneumatic actuation model vs instantaneous actuation. Example of two commands p_{des} with actuation frequency v_a=2 Hz, from initial pressure p_{ini}=0 bar. First actuation: p_{des}=2 bar (Δp=2 bar). Second actuation: p_{des}=1 bar (Δp=1 bar). The model captures the pressure transient more realistically than the instantaneous actuation considering loading and unloading times. Parameters used for the figure: p^0=0.2 bar, t_{rise}=0.2, t_{drop}=0.56, t_{delay}=0 s.

the transient pressure response within the chambers through a parameterized, third-order smooth step polynomial function

$$p(\tilde{t}) = \begin{cases} p_{ini}, & \tilde{t} \leq 0 \\ \left(3\tilde{t}^2 - 2\tilde{t}^3\right)\Delta p + p_{ini}, & 0 \leq \tilde{t} \leq 1 \\ p_{des}, & \tilde{t} \geq 1 \end{cases} \quad (28)$$

where p_{ini} and p_{des} are the initial and desired valve pressures respectively, while $\Delta p = p_{des} - p_{ini}$ is the pressure change. The variable $\tilde{t}$ is the normalized time for the current actuation, obtained by scaling and clipping the time-step t between 0 and 1, as

$$\tilde{t} = \min\left(1, \max\left(0, \frac{t - t_{delay}}{t_{max} - t_{delay}}\right)\right). \quad (29)$$

Here t_{delay} captures actuation delays caused by communication protocols and electronics, while t_{max} accounts for the time needed to reach the desired pressure

$$t_{max} = \begin{cases} dt + |\Delta p| t_{rise}, & \Delta p \geq 0 \\ dt + |\Delta p| t_{drop}, & \Delta p < 0 \end{cases} \quad (30)$$

where we defined t_{rise} and t_{drop} to be the loading and unloading times respectively for Δp=1 bar. We add the integration time-step dt to avoid division by zero when Δp=0 and t_{delay}=0. Finally, we modelled the minimum pressure command p^0 that prompts an actuation as $p \leftarrow p \cdot [p \geq p^0]$, so that there is no strain if p is less than the threshold p^0.[1] To summarize, the proposed model of the pneumatic actuation system has four parameters: t_{delay}, t_{rise}, t_{drop} and p^0. Note that the instantaneous actuation case can be reproduced by setting t_{rise}=t_{drop}=t_{delay}=0 and p^0=0 (see Fig. 4).

---

[1]Iverson bracket notation: [C] = 1 if condition C is true, 0 otherwise.

F. BOUNDARY CONDITIONS
The robot is subject to boundary conditions describing its position and orientation in the environment. The robot base is fixed at the origin of the laboratory frame, $r(0, t) = 0$, and oriented vertically downward, $Q(0, t) = \{-i, j, -k\}$.

G. INITIAL CONDITIONS
The simulations begin at time t=0 with the arm at rest in a straight configuration, unactuated and undeformed, so that $\sigma^0_{\mathcal{L}} = \kappa^0_{\mathcal{L}} = 0$ and $\sigma_{\mathcal{L}} = \kappa_{\mathcal{L}} = 0$.

H. DAMPING
The viscoelastic properties of materials are usually modeled with constitutive relations that are a function of both strain and strain rate, which increase the computational cost. Here we use an analytical linear damper, which uses the following equations to damp translational and rotational velocities

$$v_{t+1} = v_t \cdot \exp\left(-\lambda_t dt\right) \quad (31)$$

$$\omega_{t+1} = \omega_t \cdot \exp\left(-\frac{\lambda_r \rho A dt}{J}\right), \quad (32)$$

where λ_t and λ_r are the (constant) translational and rotational damping constants, respectively. This approach does not accurately model viscoelastic phenomena but it captures the overall material friction effects dissipating energy.

I. GRAVITY
The simulated environment also accounts for the self-weight of the soft arm through a uniformly distributed gravitational force $f_g = -\rho A g k$, where g is the gravitational acceleration.

J. NUMERICS
The continuous Cosserat rod model is discretized into $n + 1$ nodes connected by n cylindrical segments [36]. The rod dynamics is then computed by integrating in time the discretized set of equations via a symplectic, second-order, position Verlet scheme. This numerical integrator offers a good tradeoff between computational cost and numerical accuracy, which complies with our aim to use the model within data-driven control schemes. Rather than enforcing a rigorous Courant-Friedrichs-Levy stability condition [38], typically used with explicit time integrators, the integration time-step was selected empirically considering the arm length L, such that $dt \sim 0.01\, dl$, with $dl = L/n$ [36].

K. MODEL PARAMETERS
The soft robotic arm was modeled as a single Cosserat rod, for which several geometrical, material and numerical parameters were measured, estimated, or fitted (see Table 1).

1) GEOMETRICAL
We measured from the physical prototype the rest length of the rod L and the radial distance δ between the center of each actuator's cross-section and the centroid of the cross-section. In particular, we set L=190 mm to account for the

TABLE 1. Model parameters used in numerical simulation.

Parameter	Value	
Geometrical		
L	190	mm
$\theta_1, \theta_2, \theta_3$	90, 210, 330	°
δ	20	mm
r_o	7.79	mm
r_i	6.39	mm
Material		
m	0.1704	kg
ρ	1104	kg m^{-3}
ν	0.5	-
E	$1.6464 \cdot 10^6$	Pa
$\gamma_1, \gamma_2, \gamma_3$	1.0133, 1.0035, 1.1092	-
λ_t	806	s^{-1}
λ_r	$1.9416 \cdot 10^{-4}$	m^2 s^{-1}
Environment		
g	9.80513	m s^{-2}
Numerical		
n	20	-
dt	$2 \cdot 10^{-4}$	s
Pneumatic System		
p^0	0.2	bar
t_{rise}	0.2	s
t_{drop}	0.56	s
t_{delay}	0	s

length of the pneumatic chamber (180 mm) plus the height of the bottom terminal and the lower part of the top terminal. As shown in Fig. 2, the cross-section of each pneumatic chamber is elliptical. For simplicity, we approximated it with an annulus. The outer radius of the actuator r_o was approximated as the average of the outer radii of the external and internal ellipses constituting the chambers (see Fig. 2). Idem for the inner actuator radius, which is equivalent to subtracting the wall thickness of the chambers from the outer radius (i.e., $r_i = r_o - t_w$). The area of the interior of the actuator's cross-section was computed as $A_i = \pi r_i^2$. The cross-sectional area of the actuator was calculated as the area of the annulus, $a = \pi(r_o^2 - r_i^2)$. The effective cross-section area of the rod was then defined as $A = Na$, thus ignoring the constraining disks. We computed the second moment of area about the local axes $\boldsymbol{d}_1$ and $\boldsymbol{d}_2$ as the sum of the second moments of area of each actuator

$$I_1 = \sum_{j=1}^{N} \frac{\pi}{4}\left(r_o^4 - r_i^4\right) + a\left(\delta \sin \theta_j\right)^2 \quad (33)$$

$$I_2 = \sum_{j=1}^{N} \frac{\pi}{4}\left(r_o^4 - r_i^4\right) + a\left(\delta \cos \theta_j\right)^2. \quad (34)$$

The polar moment of area is then $I_3 = I_1 + I_2$. The actuators are disposed at angular positions

$\theta_j \in \{90, 210, 330\}$ degrees (see Fig. 2) measured from director $\boldsymbol{d}_1$. This approach considers that only the chambers resist bending and stretching, assuming no contribution from the disks.

2) MATERIAL

The total mass m of the rod was determined from the weight of the robot's components. This mass was distributed uniformly on the rod nodes so that $m = \sum_{i=0}^{n} m_i$, with m_i the node mass. The material density $\rho = 1104$ kg/m^3 was taken from the datasheet of the TPU 80 A LF by BASF^{TM}. The elastic modulus of the arm, $E = 1.646439 \cdot 10^6$ Pa, was found by fitting experimental stretching data and leveraging the analytical pressure-strain relation (24). We describe the stretching experiment in section IV and show the data in Fig. 7. Under the assumption of an incompressible material, we set the Poisson ratio to $\nu = 0.5$. The shear modulus was computed from the estimates of the elastic modulus and the Poisson ratio as $G = E/2(\nu + 1)$. Finally, the components of the strain gain matrix $\boldsymbol{\Gamma}$, as well as the translational and rotational damping constants, λ_t and λ_r, were found by solving an optimization problem as discussed below.

3) NUMERICAL

To achieve a good tradeoff between computational cost and fidelity to the continuum model and numerical stability, we discretized the rod in $n = 20$ equal segments so that $dl = 9.5$ mm. The integration time-step was set to $dt = 2 \cdot 10^{-4}$ s. This set of values allowed simulating the rod dynamics about 2.5 times faster than in real-time on a laptop (Intel i7-1165G7 @ 2.80 GHz Processor, 8 GB RAM).

4) PNEUMATIC SYSTEM

For the parameters of the pneumatic actuation system, we empirically found using a manometer that the minimum pressure to activate the valves is $p^0 = 0.2$ bar. The delay of the communication protocols and electronic signals was assumed to be negligible, hence $t_{delay} = 0$ s. To determine the load time t_{rise} and unload time t_{drop}, we used data obtained from a test performed by the manufacturer of the pressure control system. The test measured the response time to go from 0 bar to 5 bar ($\Delta p = 5$ bar) for a volume $V_{test} = 10^{-5}$ m^3 using proportional pressure-controlled electronic valves (Mod. K8P-0-D522-0, Working pressure: 0-10 bar by Camozzi Automation) with input pressure 11 bar. The results obtained were approximately 0.5 s and 1.4 s for loading and unloading, respectively. We assumed a linear relationship between Δp and load/unload time and a linear relationship between controlled volume and load/unload time. Note that the internal volume of the pneumatic chamber, $V \sim A_i L = \pi r_i^2 L = 2.44 \cdot 10^{-5}$ m^3, is approximately twice as $V_{test} = 10^{-5}$ m^3. Therefore, we set $t_{rise} = 0.2$ s and $t_{drop} = 0.56$ s.

L. MODEL OPTIMIZATION

To jointly estimate the actuator strain gains, $\boldsymbol{\gamma} = (\gamma_1, \gamma_2, \gamma_3)$, and the damping constants λ_t and λ_r, the following

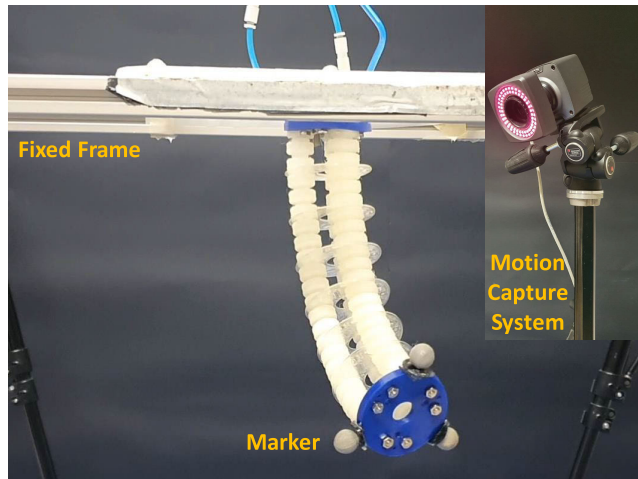**FIGURE 5.** Experimental setup.

constrained optimization problem was formulated and solved

$$\min_{\boldsymbol{\gamma}, \lambda_t, \lambda_r} \quad \sum_{\mathcal{D}_i \in \mathcal{D}} \frac{1}{|\mathcal{D}_i|} \sum_{t=0}^{T_i} ||\boldsymbol{e}(t; \boldsymbol{\gamma}, \lambda_t, \lambda_r)||^2$$

$$\text{subject to} \quad \gamma_1 - \gamma_3 < 0$$
$$\gamma_2 - \gamma_3 < 0$$
$$2\gamma_1 - \gamma_2 - \gamma_3 < 0$$
$$0.9 \le \gamma_i \le 1.2 \qquad i = 1,2,3$$
$$0 \le \lambda_t \le 2 \cdot 10^3$$
$$0 \le \lambda_r \le 10^{-2}. \tag{35}$$

Here $\mathcal{D}$ is the collection of datasets used to optimize the decision variables, T_i is the duration of each time series, and $\boldsymbol{e}(t) = \boldsymbol{r}_{data}(t) - \boldsymbol{r}(t, L)$ is the difference between the measured and simulated position of the free end of the robot. The optimization was conducted on three datasets (stretching, bending 1, bending 2) described in section IV. The constraints on the strain gains were obtained by observing the stretching and bending experimental data. The optimization problem was solved with a Trust Region method implemented in *scipy.optimize*. An analytical expression of the gradient of the cost function with respect to the decision variables was not readily available, so it was estimated with a 2-point finite difference. The Hessian was approximated via the BFGS strategy. The initial solution of the optimization was set to $(\boldsymbol{\gamma}, \lambda_t, \lambda_r) = (\mathbf{1}, 10^3, 10^{-3})$. Optimization for 30 iterations resulted in $\boldsymbol{\gamma} = (1.0133, 1.0035, 1.1092)$, $\lambda_t = 806 \text{ s}^{-1}$ and $\lambda_r = 1.9416 \cdot 10^{-4} \text{ m}^2 \text{ s}^{-1}$.

IV. EXPERIMENTS

A. EXPERIMENTAL SETUP
The AM I-Support robotic platform was oriented vertically downward with the top terminal fixed to a plexiglass frame and placed upon a rectangular support (see Fig. 5). Three proportional pressure-controlled electronic valves (Mod. K8P-0-D522-0 by Camozzi Automation, Working pressure:

0−10 bar) actuated the pneumatic chambers. A stand-alone air compressor set at 6 bar pressure provided the air source to the valves. An Arduino Due board and a custom electronic board controlled the valves. The Vicon motion capture system with eight infrared cameras (100 fps) collected the position trajectories of six reflective markers. Three markers on top of the support defined the global reference frame with the origin at the support center. The other three markers were attached to the end-effector aligned with the pneumatic chambers.

B. EXPERIMENTAL PROTOCOL
First, the pneumatic chambers were subject to the same load-unload cycle for pressure inputs from $p_{min}=0$ bar to $p_{max}=3.5$ bar, with steps of $\Delta p=0.5$ bar, to mitigate the Mullins effect. Then, the soft robotic arm collected motion data in various conditions to validate the model experimentally. The input pressures were varied with actuation frequency v_a, while the markers' positions were read from the motion capture system with sampling frequency v_s. The actuation patterns are the following:
1) **Stretching**: Actuate three chambers simultaneously with equal increasing pressure values, from p_{min} to p_{max} with $\Delta p=0.5$ bar; $v_a=0.2$ Hz, $v_s=100$ Hz.
2) **Bending with 1 chamber**: Actuate one chamber with increasing pressure values, from p_{min} to p_{max} with $\Delta p=0.5$ bar; repeat for the other two chambers in sequence; $v_a=0.2$ Hz, $v_s=100$ Hz.
3) **Bending with 2 chambers**: Actuate two chambers simultaneously with equal increasing pressure values, from p_{min} to p_{max} with $\Delta p=0.5$ bar; repeat for the other two combinations of two chambers in sequence; $v_a=0.2$ Hz, $v_s=100$ Hz.
4) **Workspace**: Actuate three chambers with all 512 dispositions with repetitions of pressure values in the interval $[p_{min}, p_{max}]$ with $\Delta p=0.5$ bar; $v_a=0.2$ Hz, $v_s=0.2$ Hz (i.e., only the quasi-static position is saved).
5) **Motor Babbling**: Actuate three chambers for 5 minutes with pseudo-random commands generated by a random walk in the three-dimensional pressure space, with $\Delta p \in \{-0.05, 0, 0.05\}$ bar uniformly sampled. Formally, $p(t) = p(t - 1) + \Delta p$, with $p(0)=0$. Five different actuation patterns were generated with $v_a \in \{1, 2, 5, 10, 20\}$ Hz, $v_s=100$ Hz (see Fig. 6).
6) **Sinusoids**: Actuate three chambers for 20 seconds with three sinusoidal inputs shifted by phases $\phi_i = \{0, 2/3\pi, 4/3\pi\}$. Three datasets were generated with ordinary frequency $f \in \{0.05, 0.1, 0.2\}$ Hz, $v_a=20$ Hz, $v_s=100$ Hz. The sinusoids had amplitude $A_p=1.5$ bar and offset by $p_{off}=2$ bar. Formally, $p_i(t) = p_{off} + A_p \cdot \sin(2\pi f t + \phi_i)$.

Each experiment consisted of three trials to capture the variability of the actuation system and the material response. Interleaving the trials with rest periods proportional to the trial duration allowed the soft material to restore the original rest configuration. In this way, the standard deviation of the experimental data was less than a millimeter and, for
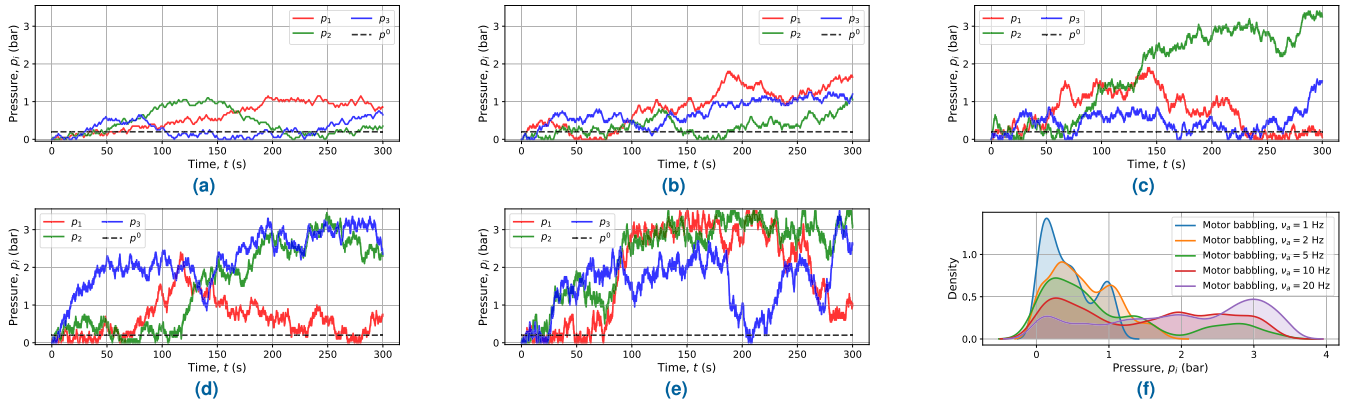
FIGURE 6. Pressure commands for motor babbling motion at different actuation frequency ν_a. (a) 1 Hz, (b) 2 Hz, (c) 5 Hz, (d) 10 Hz, (e) 20 Hz. Pressure threshold p^0=0.2 bar is shown. (f) Distribution of pressure commands highlights how the tasks differ in terms of actuations explored.

TABLE 2. Quasi-static model validation.

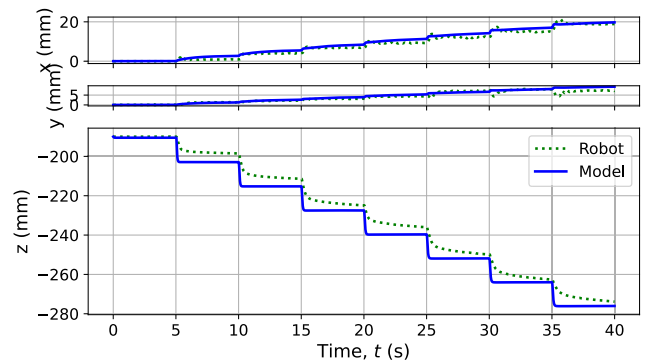| Experiment	$|e_x|$ (mm)	$|e_y|$ (mm)	$|e_z|$ (mm)	e/L (%)
Stretching	1.4	0.6	2.6	1.6 ± 0.6
Bending 1	4.8	5.2	3.9	4.8 ± 2.2
Bending 2	3.7	5.1	5.9	5.5 ± 2.5
Workspace	9.1	5.2	7.0	7.4 ± 4.1

FIGURE 7. Robot vs model tip trajectories for the stretching experiment. The x-y displacements caused by actuators irregularities are captured by tuning the strain gains γ_i.

simplicity, is not reported. Text files stored the pressure commands and markers' trajectories after each trial.

Then, the trajectories of the three markers attached to the tip were post-processed. The centroid of the three markers reconstructed the centerline of the end-effector, $\boldsymbol{r}_{data}(t)$. Subsequently, the data were translated so that the rest position of the end-effector was $(x, y, z) = (0, 0, -L)$. Finally, the data were rotated around the z-axis so that one actuator aligns with the positive y-axis (director $\boldsymbol{d}_2$). After post-processing, each dataset consisted of a sequence of commands $\boldsymbol{p}(t)$ and tip positions $\boldsymbol{r}_{data}(t)$ for the model validation.

V. EXPERIMENTAL VALIDATION
An extensive experimental validation conducted in quasi-static and dynamic conditions assessed how well the model describes the mechanics of the soft robot. The real and the simulated robots were subject to the same input pressures with actuation frequency ν_a depending on the experiment. Then, the end-effector trajectories of the soft robotic arm and the model, respectively $\boldsymbol{r}_{data}$ and $\boldsymbol{r}(L)$, were collected with sampling frequency ν_s=100 Hz. Subsequently, we computed the Euclidean distance between the end-effector positions at each time step, $\boldsymbol{e}(t) = \boldsymbol{r}_{data}(t) - \boldsymbol{r}(L, t)$. The used performance metric was the mean and standard deviation of the norm of the tip error normalized to the arm length, e/L. In addition, to better analyze the pros and limitations of the model, we reported the mean component-wise absolute error

on each axis, $|e_x|$, $|e_y|$, and $|e_z|$. The error calculation omits the sub-millimeter fluctuations of the motion capture system.

A. QUASI-STATIC VALIDATION
The model reproduced the experimental data of the four quasi-static actuation patterns with a mean tip error of 4.83%L (about 9.2 mm). In particular, the model achieved an average tip error of 1.6%L, 4.8%L, and 5.5%L on the main motion patterns (i.e., stretching, bending 1, bending 2); and 7.4%L on the quasi-static workspace (see Table 2).

As shown in Fig. 7, the stretching motion produces non-negligible bending displacements in the x-y plane. The displacements result from unequal elongations of the chambers and increase with higher pressure values. Thanks to the strain gains of the actuators introduced in section III-D, the model was able to obtain minimal average quasi-static errors (i.e., $|e_x|$=1.4 mm, $|e_y|$=0.6 mm in Table 2). Without strain grains, the errors would rise to about 20 mm on the x-axis and about 10 mm on the y-axis for high-pressure values.

The model reproduced the overall bending deformations successfully. In particular, the strain gains contributed to capturing the different peak displacements along the z-axis
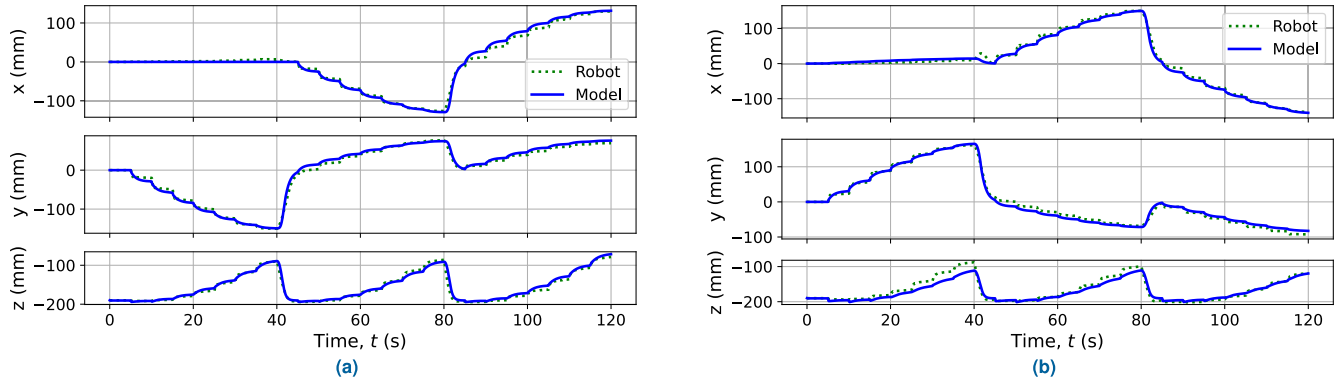
FIGURE 8. Robot vs model tip trajectories for the bending experiments. (a) Single chambers are actuated in sequence (I; II; III); (b) Pairs of chambers are actuated in sequence (II&III; I&III; I&II). At two relaxation periods at $t=40$ and $t=80$, the pressure command vanishes, $p_i=0$, and the actuated chambers change. The strain gains γ_i help to adjust the peaks on the z-axis.
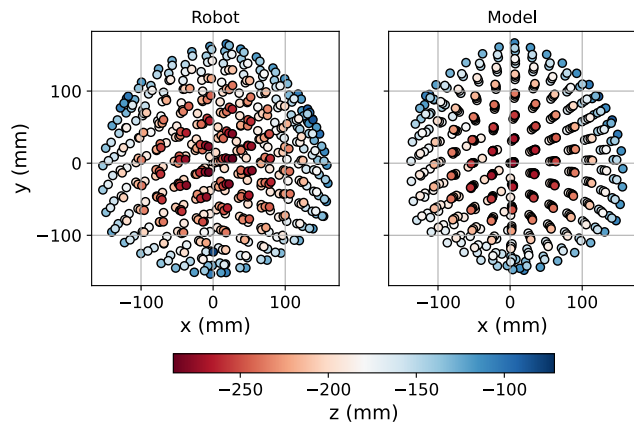

FIGURE 9. Robot vs model quasi-static workspace. Robot range: 312 mm × 319 mm × 210 mm; model range: 293 mm × 315 mm × 205 mm. Combining damping and strain gains reproduces the workspace asymmetries.

TABLE 3. Dynamic model validation.

Experiment	ν_a (Hz)	$|e_x|$ (mm)	$|e_y|$ (mm)	$|e_z|$ (mm)	e/L (%)
Stretching	0.2	1.0	0.6	4.1	2.3 ± 1.2
Bending 1	0.2	4.2	4.7	3.7	4.4 ± 2.8
Bending 2	0.2	4.3	5.5	7.3	6.3 ± 3.2
Motor Babbling	1	3.8	4.1	1.7	3.5 ± 1.6
	2	3.5	5.5	2.2	4.1 ± 1.5
	5	6.3	3.4	9.9	7.2 ± 3.8
	10	5.6	4.4	9.0	6.9 ± 3.4
	20	6.8	6.6	5.5	6.5 ± 3.5
Sinusoids ($f=0.05$ Hz)	20	26.4	10.2	15.9	18.4 ± 12.3
Sinusoids ($f=0.10$ Hz)	20	27.0	22.9	19.0	23.3 ± 11.1
Sinusoids ($f=0.20$ Hz)	20	25.6	33.2	15.9	25.9 ± 11.2

when single chambers were actuated (see Fig. 8a). However, as shown in Fig. 8b, capturing the different bending peaks actuating two chambers is more challenging.

Finally, the simulated and experimental data had more pronounced discrepancies in the quasi-static workspace experiment. This result was mainly due to the slow viscoelastic relaxation of the TPU and hysteresis effects, which keep the chamber deformed during long trials. Indeed, after a workspace exploration, several hours were required between successive trials for the robot to return to its resting position. Nonetheless, Fig. 9 shows that the model reproduced the overall shape of the robot workspace.

B. DYNAMIC VALIDATION

For the principal stretching and bending motions, the model achieved an average dynamic tip error of 4.33%L, respectively 2.3%L, 4.4%L, and 6.3%L (see Table 3). Despite the low average error, as shown in Fig. 7, the model did not perfectly capture the transient behavior on the z-axis in the stretching experiment. The time series of the tip

error presented spikes in the time steps corresponding to the pressure changes (see supplementary material). This problem could be mitigated by considering dynamics effects more comprehensively, for example, by employing non-linear constitutive laws in conjunction with more precise pressure-transient models. Future work could address this to reduce the real-to-sim gap. For the damping mechanism adopted, the dynamic response depends on the damping constants λ_t and λ_r. The model could achieve a qualitatively finer dynamic behavior on the stretching motion by setting large translational damping constants (e.g., $\lambda_t \sim 5000$ found empirically). However, such high values of λ_t would negatively affect the bending deformation of the rod and the accuracy attained on the bending patterns. Therefore, optimizing the damping constants jointly on the stretching and bending motions was a reasonable tradeoff for an adequate average performance.

The average dynamic tip error in the motor babbling experiments was 5.64%L, ranging from 3.5%L to 7.2%L (see Table 3). Although the actuation frequency was approximately doubled from one experiment to another, the average tip error did not follow a strictly increasing trend. Moreover, the solutions for γ, λ_t and λ_r found by optimizing on the principal motions of stretching and bending, with actuation frequency $\nu_a=0.2$ Hz, generalized to the rest of the experimental motor babbling data, which
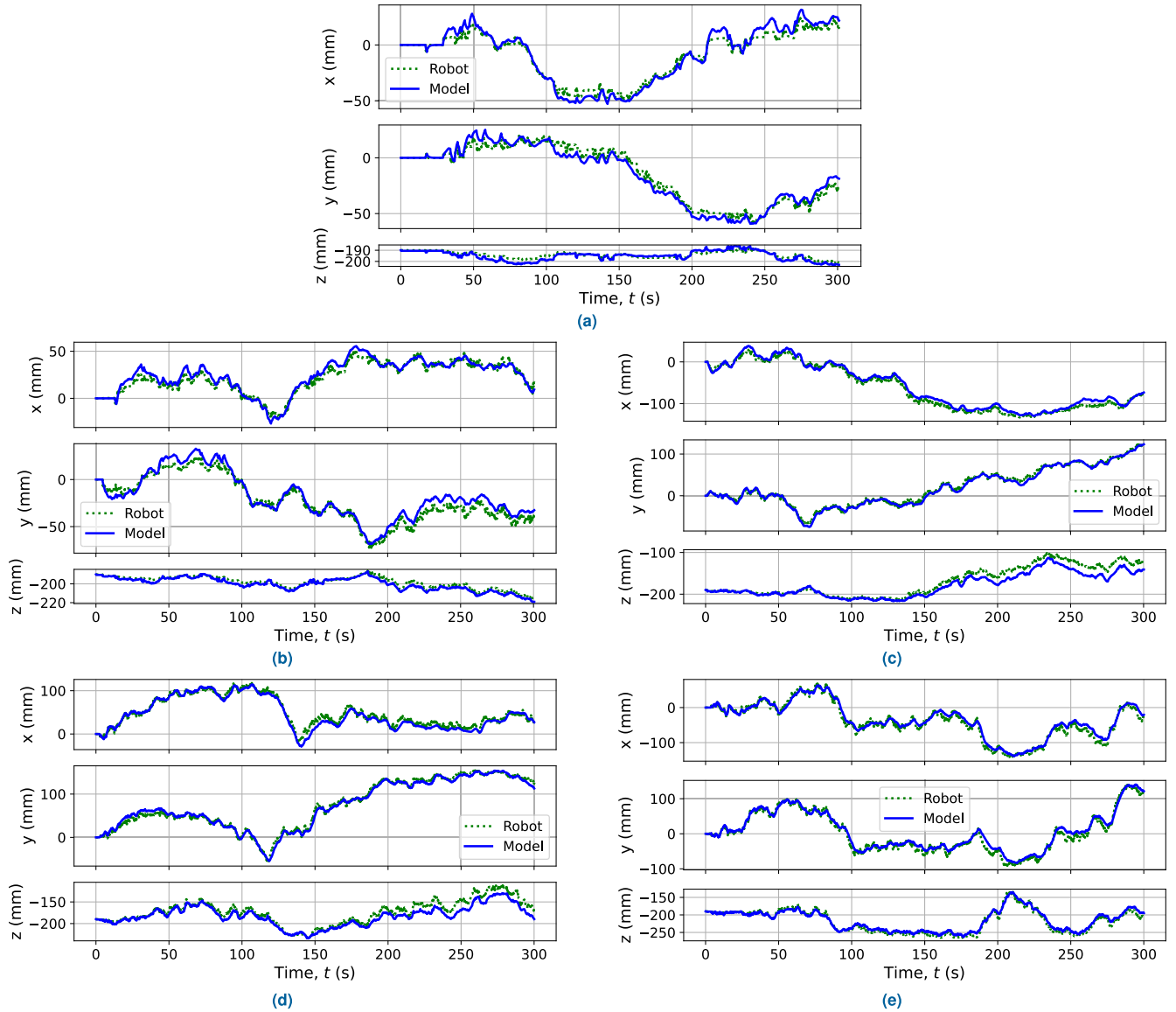
FIGURE 10. Robot vs model tip trajectories for the motor babbling experiments with actuation frequencies (a) 1 Hz, (b) 2 Hz, (c) 5 Hz, (d) 10 Hz, and (e) 20 Hz. The pressure threshold p^0 helps in capturing the first few seconds of inactivity as visible in experiments (a) and (b).

have actuation frequencies between 5 and 100 times higher. Therefore, the model is robust to a wide range of actuation frequencies, while the performance difference in the motor babbling patterns is mainly due to the different actuation distributions (see Fig. 6) and how well the pressure-strain relation $\epsilon(p)$ matches experimental data in different pressure intervals (see Fig. 3). Overall, the model tracked the complex pseudo-random motions of the soft robot satisfactorily, as shown in Fig. 10.

For the sinusoidal motions, the average tip error was 22.53%L, ranging between 18.4%L and 25.9%L (see Table 3). Big error spikes at the beginning of the experiments contributed to the high average error in the sinusoidal pattern. The error spikes were due to initial pressure commands greater than 2 bar as a result of the high offset and amplitude

parameters (p_{off}=2 bar, A_p=1.5 bar). Qualitatively, the model reproduced the first slow sinusoidal motion well but could not capture the sine amplitudes as accurately for faster movements. The same argument about the damping coefficients made for the bending patterns applies. Nonetheless, the model could achieve greater accuracy on all motion patterns using a finer spatiotemporal discretization (e.g., $n\sim100$) and optimizing more parameters on all datasets. See more details on these experiments in the supplementary material.

VI. ABLATION STUDY: FULL MODEL VS VARIATIONS
To understand how different model components contribute to the overall performance, we conducted an ablation study evaluating four model variations obtained by removing or degrading a feature of the proposed model (i.e., the Full
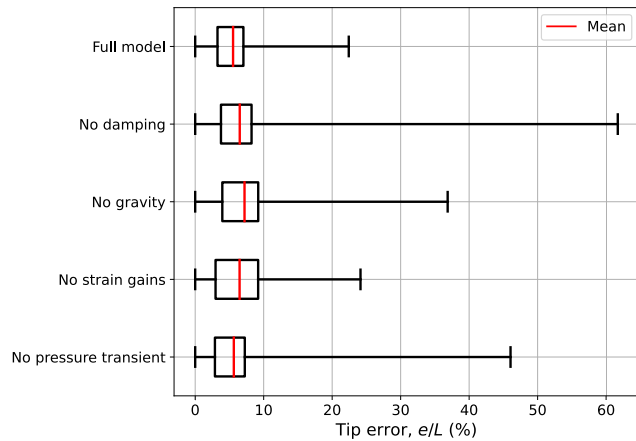
FIGURE 11. Ablation study: Full model vs ablated models. Each box plot was created from the tip error collection obtained by the corresponding model variation evaluated in the eight dynamic experiments. Whiskers show the minimum and maximum errors over time.

TABLE 4. Ablation study: average tip error difference Δe (%) between the ablated models and the full model.

Experiment	ν_a (Hz)	No Damping	No Gravity	No Strain gains	No Pressure transient
Stretching	0.2	0.2	0.47	3.13*	0.06
Bending 1	0.2	3.43	5.08*	-0.41	1.03
Bending 2	0.2	1.47	2.79*	2.13	1.42
Motor Babbling	1	0.45	1.54*	-0.48	-0.61
	2	0.58	0.67*	-0.53	-0.33
	5	0.16	-2.27	-0.75	0.3*
	10	0.91	2.02	5.15*	0.22
	20	1.7	4.77*	1.17	0.08
Mean Δe (%)		1.11	1.88	1.18	0.27

* indicates for each experiment the component with the highest influence.

model). We tested the ablated models on eight dynamic motion patterns and compared their performance against the Full model. As a metric, we computed the difference of the average tip errors $\Delta e = (\tilde{e} - e)/L$, where $\tilde{e}$ is the average tip error of the degraded model. In addition, for each model version, we measured the spread of the tip errors with the interquartile range (IQR) and the maximum error.

In particular, we evaluated the impact of the strain gains by setting $\gamma = 1$, which is equivalent to assuming that the pneumatic chambers have the same behavior when pressurized. Another test evaluated the effect of degraded damping (λ_t=10, λ_r=10^{-6}), which reduced energy dissipation. Note that we could not thoroughly assess the zero-damping case (λ_t=λ_r=0) because the oscillations of the undamped system caused numerical instability in several experiments. The ablation of the pneumatic actuation model (p^0=0, t_{rise}=dt, t_{drop}=dt, t_{delay}=0) resulted in instantaneous pressure changes. Finally, setting the gravitational acceleration to g=0 neglected the effects of self-weight.

As reported in Fig. 11 and Table 4, the Full model outperformed all the ablated models in every performance metric. In particular, the model without strain gains presented the highest error dispersion around the median. Moreover, the models with degraded damping and instantaneous pressure changes produced very high maximum tip errors (above 40%L). In terms of differences in the average tip error, the most influential component was gravity (Δe=1.88%L), followed by the strain gains (Δe=1.18%L) and damping (Δe=1.11%L), and finally the pressure transient (Δe=0.27%L) (see Table 4).

A. EFFECT OF ACTUATOR STRAIN GAINS
The contribution of the strain gains was more pronounced in the motions that generated severe stretching (e.g., in stretching pattern Δe=3.13%L), where capturing the deviations on the x-y plane is crucial. Moreover, the strain gains contributed

significantly in the experiments that actuate high pressures in the most stretchable chamber (i.e., the actuator with the highest γ_i). Indeed, as shown in Fig. 6d (motor babbling at 10 Hz), the third actuator with γ_3=1.1092 is very solicited compared to the others, so that Δe=5.15%L when omitting the strain gains. The few negative Δe for the no strain gains case are perhaps due to the low contribution of the third actuator and minor unmodeled effects.

B. EFFECT OF PRESSURE TRANSIENT
The effect of the pneumatic actuation model was sensible in terms of Δe only in the principal bending experiments, with Δe=1.03%L and Δe=1.42%L, respectively. As shown in Fig. 8, this was because these patterns included two unloading phases characterized by a significant pressure drop of Δp=3.5 bar when switching the pressurized chamber. For the pseudo-random experiments, the pneumatic actuation model was useful to capture the first few seconds of inactivity thanks to the actuation threshold p^0 (see motor babbling at 1 Hz and 2 Hz in Fig. 10). However, the overall contribution in these experiments was less visible because the pressure steps of Δp=0.05 bar were small enough to be approximated as instantaneous. Nonetheless, relative to the motor babbling experiments, the pressure transient contribution was higher in the case of 5 Hz and 10 Hz. As shown in Fig. 6c and Fig. 6d, the input pressure profiles are characterized by long series of pressure decreases. Our simplified model of pneumatic actuation can capture this phenomenon through the t_{drop} parameter, which is greater than the time of pressure build-up t_{rise}. Therefore, we conclude that the pressure transient component is significant for big negative pressure changes.

C. EFFECT OF DAMPING
The damping component, similar to the pneumatic actuation model, contributes to the overall system dynamics. However, the damping component is significant for fast actuation changes regardless of the sign of Δp. As shown in Table 4, also the contribution of damping was higher in the bending experiments, which presented significant negative pressure changes, as discussed before. Damping had a non-negligible effect also on the motor babbling experiment at 20 Hz.

As shown in Fig. 6e, there are some time-step intervals in which the derivative of the actuation profile is high.

D. EFFECT OF GRAVITY

The removal of gravity had a more severe effect when the bending deformation of the arm was significant, as in the case of the bending experiments and the motor babbling at 20 Hz, because bending moments generated by self-weight were neglected by this ablated model. Conversely, the effect of gravity was negligible in the stretching experiment. Notice that for the motor babbling at 5 Hz the ablated model performed better than the full model. The reason for this unexpected result is not very clear by observing the pressure profile and distribution in Fig. 6.

VII. CONCLUSION

This paper presented a dynamic Cosserat rod model for a 3D-printed pneumatic soft robotic arm. The model considers actuators' irregularities by tuning the pressure-strain relation for each pneumatic chamber. In addition, it includes a simplified model of the pneumatic actuation system that captures the time-dependent response of proportional pressure-controlled electronic valves. A comprehensive experimental validation on several actuation patterns characterized by different pressure profiles and actuation frequencies resulted in a mean quasi-static tip error of 9.2 mm (4.83% of the arm length) and a mean dynamic tip error of 18.8 mm (9.9% of the arm length). From an ablation study of the model components, it emerged that the most influential factors are gravity and the strain gains, followed by damping and pressure transient. In addition, the specific contribution varies from experiment to experiment. In particular, tuning the pressure-strain relation of the actuators using strain gains is most effective when the actuator with relatively higher stretching capability is subject to higher pressures; damping and the pressure transient are most effective when the derivative of the input actuation has a high magnitude; whereas gravitational effects are more pronounced when the deflection caused by bending is significant.

Future work will include the modeling and experimental validation of a multi-section AM I-Support, described by a sequence of Cosserat rods connected by fixed joints. Careful calibration of the single-section model could likely result in satisfactory performance in the multi-section case [39]. Other extensions could explore more refined damping mechanisms and a more comprehensive validation of the pneumatic system model. Decoupling the transient response of the actuation systems from the viscoelastic behavior of soft materials could enable a better characterization of both components to develop more accurate dynamic soft robot models. Finally, a further investigation of strain gains in soft actuators could capture, in addition to manufacturing irregularities, material deterioration, and damage. This ability could soon serve the next generation of soft robots incorporating self-healing [40].

REFERENCES

[1] C. Laschi, B. Mazzolai, and M. Cianchetti, "Soft robotics: Technologies and systems pushing the boundaries of robot abilities," *Sci. Robot.*, vol. 1, no. 1, Dec. 2016, Art. no. eaah3690.

[2] D. Rus and M. T. Tolley, "Design, fabrication and control of soft robots," *Nature*, vol. 521, pp. 467–475, May 2015.

[3] C. Laschi and M. Cianchetti, "Soft robotics: New perspectives for robot bodyware and control," *Frontiers Bioeng. Biotechnol.*, vol. 2, p. 3, Jan. 2014.

[4] C. Armanini, F. Boyer, A. T. Mathew, C. Duriez, and F. Renda, "Soft robots modeling: A structured overview," *IEEE Trans. Robot.*, early access, Jan. 6, 2023, doi: 10.1109/TRO.2022.3231360.

[5] T. G. Thuruthel, Y. Ansari, E. Falotico, and C. Laschi, "Control strategies for soft robotic manipulators: A survey," *Soft Robot.*, vol. 5, no. 2, pp. 149–163, Apr. 2018.

[6] K. Chin, T. Hellebrekers, and C. Majidi, "Machine learning for soft robotic sensing and control," *Adv. Intell. Syst.*, vol. 2, no. 6, Jun. 2020, Art. no. 1900171.

[7] A. Melingui, C. Escande, N. Benoudjit, R. Merzouki, and J. B. Mbede, "Qualitative approach for forward kinematic modeling of a compact bionic handling assistant trunk," *IFAC Proc. Volumes*, vol. 47, no. 3, pp. 9353–9358, 2014.

[8] A. Centurelli, L. Arleo, A. Rizzo, S. Tolu, C. Laschi, and E. Falotico, "Closed-loop dynamic control of a soft manipulator using deep reinforcement learning," *IEEE Robot. Autom. Lett.*, vol. 7, no. 2, pp. 4741–4748, Apr. 2022.

[9] F. Pique, H. T. Kalidindi, L. Fruzzetti, C. Laschi, A. Menciassi, and E. Falotico, "Controlling soft robotic arms using continual learning," *IEEE Robot. Autom. Lett.*, vol. 7, no. 2, pp. 5469–5476, Apr. 2022.

[10] V. K. Venkiteswaran, J. Sikorski, and S. Misra, "Shape and contact force estimation of continuum manipulators using pseudo rigid body models," *Mechanism Mach. Theory*, vol. 139, pp. 34–45, Sep. 2019.

[11] H. Habibi, C. Yang, I. S. Godage, R. Kang, I. D. Walker, and D. T. Branson, "A lumped-mass model for large deformation continuum surfaces actuated by continuum robotic arms," *J. Mech. Robot.*, vol. 12, no. 1, Feb. 2020, Art. no. 011014.

[12] C. D. Santina and D. Rus, "Control oriented modeling of soft robots: The polynomial curvature case," *IEEE Robot. Autom. Lett.*, vol. 5, no. 2, pp. 290–298, Apr. 2020.

[13] Q. Xie, T. Wang, and S. Zhu, "Simplified dynamical model and experimental verification of an underwater hydraulic soft robotic arm," *Smart Mater. Struct.*, vol. 31, no. 7, Jul. 2022, Art. no. 075011.

[14] R. J. Webster and B. A. Jones, "Design and kinematic modeling of constant curvature continuum robots: A review," *Int. J. Robot. Res.*, vol. 29, no. 13, pp. 1661–1683, Jun. 2010.

[15] E. Coevoet, T. Morales-Bieze, F. Largilliere, Z. Zhang, M. Thieffry, M. Sanz-Lopez, B. Carrez, D. Marchal, O. Goury, and J. Dequidt, "Software toolkit for modeling, simulation, and control of soft robots," *Adv. Robot.*, vol. 31, no. 22, pp. 1208–1224, 2017.

[16] M. S. Xavier, A. J. Fleming, and Y. K. Yong, "Finite element modeling of soft fluidic actuators: Overview and recent developments," *Adv. Intell. Syst.*, vol. 3, no. 2, Feb. 2021, Art. no. 2000187.

[17] J. Allard, S. Cotin, F. Faure, P.-J. Bensoussan, F. Poyer, C. Duriez, H. Delingette, and L. Grisoni, "Sofa—An open source framework for medical simulation," in *MMVR 15-Medicine Meets Virtual Reality*, vol. 125. Beijing, China: IOP Press, 2007, pp. 13–18.

[18] M. Dubied, M. Y. Michelis, A. Spielberg, and R. K. Katzschmann, "Sim-to-real for soft robots using differentiable FEM: Recipes for meshing, damping, and actuation," *IEEE Robot. Autom. Lett.*, vol. 7, no. 2, pp. 5015–5022, Apr. 2022.

[19] J. Till, V. Aloi, and C. Rucker, "Real-time dynamics of soft and continuum robots based on Cosserat rod models," *Int. J. Robot. Res.*, vol. 38, no. 6, pp. 723–746, May 2019.

[20] B. A. Jones, R. L. Gray, and K. Turlapati, "Three dimensional statics for continuum robotics," in *Proc. IEEE/RSJ Int. Conf. Intell. Robots Syst.*, Oct. 2009, pp. 2659–2664.

[21] D. C. Rucker and R. J. Webster, III, "Statics and dynamics of continuum robots with general tendon routing and external loading," *IEEE Trans. Robot.*, vol. 27, no. 6, pp. 1033–1044, Dec. 2011.

[22] F. Renda, M. Cianchetti, M. Giorelli, A. Arienti, and C. Laschi, "A 3D steady-state model of a tendon-driven continuum soft manipulator inspired by the octopus arm," *Bioinspiration Biomimetics*, vol. 7, no. 2, Jun. 2012, Art. no. 025006.

[23] F. Renda, M. Giorelli, M. Calisti, M. Cianchetti, and C. Laschi, "Dynamic model of a multibending soft robot arm driven by cables," *IEEE Trans. Robot.*, vol. 30, no. 5, pp. 1109–1122, Oct. 2014.

[24] J. Till, V. Aloi, K. E. Riojas, P. L. Anderson, R. J. Webster, III, and C. Rucker, "A dynamic model for concentric tube robots," *IEEE Trans. Robot.*, vol. 36, no. 6, pp. 1704–1718, Dec. 2020.

[25] A. Doroudchi, R. Khodambashi, A. S. Lafmejani, D. M. Aukes, and S. Berman, "Dynamic modeling of a hydrogel-based continuum robotic arm with experimental validation," in *Proc. 3rd IEEE Int. Conf. Soft Robot. (RoboSoft)*, May 2020, pp. 695–701.

[26] D. Trivedi, A. Lotfi, and C. D. Rahn, "Geometrically exact models for soft robotic manipulators," *IEEE Trans. Robot.*, vol. 24, no. 4, pp. 773–780, Aug. 2008.

[27] N. K. Uppalapati, G. Singh, and G. Krishnan, "Parameter estimation and modeling of a pneumatic continuum manipulator with asymmetric building blocks," in *Proc. IEEE Int. Conf. Soft Robot. (RoboSoft)*, Apr. 2018, pp. 528–533.

[28] H. B. Gilbert and I. S. Godage, "Validation of an extensible rod model for soft continuum manipulators," in *Proc. 2nd IEEE Int. Conf. Soft Robot. (RoboSoft)*, Apr. 2019, pp. 711–716.

[29] S. R. Eugster, J. Harsch, M. Bartholdt, M. Herrmann, M. Wiese, and G. Capobianco, "Soft pneumatic actuator model based on a pressure-dependent spatial nonlinear rod theory," *IEEE Robot. Autom. Lett.*, vol. 7, no. 2, pp. 2471–2478, Apr. 2022.

[30] V. Falkenhahn, T. Mahl, A. Hildebrandt, R. Neumann, and O. Sawodny, "Dynamic modeling of bellows-actuated continuum robots using the Euler–Lagrange formalism," *IEEE Trans. Robot.*, vol. 31, no. 6, pp. 1483–1496, Dec. 2015.

[31] V. Falkenhahn, A. Hildebrandt, R. Neumann, and O. Sawodny, "Dynamic control of the bionic handling assistant," *IEEE/ASME Trans. Mechatronics*, vol. 22, no. 1, pp. 6–17, Feb. 2017.

[32] C. Chen, W. Tang, Y. Hu, Y. Lin, and J. Zou, "Fiber-reinforced soft bending actuator control utilizing on/off valves," *IEEE Robot. Autom. Lett.*, vol. 5, no. 4, pp. 6732–6739, Oct. 2020.

[33] M. Stolzle and C. D. Santina, "Piston-driven pneumatically-actuated soft robots: Modeling and backstepping control," *IEEE Control Syst. Lett.*, vol. 6, pp. 1837–1842, 2022.

[34] L. Arleo, G. Stano, G. Percoco, and M. Cianchetti, "I-support soft arm for assistance tasks: A new manufacturing approach based on 3D printing and characterization," *Prog. Additive Manuf.*, vol. 6, no. 2, pp. 243–256, May 2021.

[35] M. Manti, A. Pratesi, E. Falotico, M. Cianchetti, and C. Laschi, "Soft assistive robot for personal care of elderly people," in *Proc. 6th IEEE Int. Conf. Biomed. Robot. Biomechatronics (BioRob)*, Jun. 2016, pp. 833–838.

[36] M. Gazzola, L. H. Dudte, A. G. McCormick, and L. Mahadevan, "Forward and inverse problems in the mechanics of soft filaments," *Roy. Soc. Open Sci.*, vol. 5, no. 6, Jun. 2018, Art. no. 171628.

[37] X. Zhang, F. K. Chan, T. Parthasarathy, and M. Gazzola, "Modeling and simulation of complex dynamic musculoskeletal architectures," *Nature Commun.*, vol. 10, no. 1, p. 4825, Oct. 2019.

[38] R. Courant, K. Friedrichs, and H. Lewy, "On the partial difference equations of mathematical physics," *IBM J. Res. Develop.*, vol. 11, no. 2, pp. 215–234, Mar. 1967.

[39] M. Wiese, B.-H. Cao, and A. Raatz, "Towards accurate modeling of modular soft pneumatic robots: From volume FEM to Cosserat rod," in *Proc. IEEE/RSJ Int. Conf. Intell. Robots Syst. (IROS)*, Oct. 2022, pp. 9371–9378.

[40] S. Terryn, J. Brancart, D. Lefeber, G. Van Assche, and B. Vanderborght, "Self-healing soft pneumatic robots," *Sci. Robot.*, vol. 2, no. 9, Aug. 2017, Art. no. eaan4268.

CARLO ALESSI received the B.Sc. degree in computer science and the M.Sc. degree in artificial intelligence from the University of Pisa, Pisa, Italy, in 2017 and 2019, respectively. He is currently pursuing the Ph.D. degree in biorobotics with The BioRobotics Institute, Scuola Superiore Sant'Anna (SSSA), Pisa. He was Visiting Student with the University of Bristol, U.K., in 2016; the University of Barcelona, Spain, in 2018; and the Technical University of Munich, Germany, in 2019. He was an intern Software Engineer with Nokia, Bristol, in 2017; a Research Assistant in soft robotics with SSSA, in 2020, and a visiting Ph.D. student with the Bristol Robotics Laboratory, in 2022. His research interest includes the application of machine learning algorithms to robotics, including the modeling and control of soft manipulators.

EGIDIO FALOTICO (Member, IEEE) received the M.Sc. degree in computer science from the University of Pisa, Pisa, Italy, in 2008, and the dual Ph.D. degree in innovative technologies from Scuola Superiore Sant'Anna, Pisa, and in cognitive science from Pierre et Marie Curie University Paris, France, in 2013. He is currently a tenure-track Assistant Professor with The BioRobotics Institute, Scuola Superiore Sant'Anna. He is also the Head of the BRAin-Inspired Robotics (BRAIR) Laboratory, The BioRobotics Institute. Since his early studies, he has developed a strong interest in the domain of neuroscience, and through his double Ph.D. degree, he had the chance to explore the potential of neuroscience knowledge applied to robotics. He has also put into practice his deep expertise in artificial intelligence and computational neuroscience for the control of soft and rigid robots. He serves as a PI for Scuola Superiore Sant'Anna in some European projects, such as Proboscis, GrowBot, and Human Brain Project.

ALESSANDRO LUCANTONIO received the M.Sc. degree in space engineering and the Ph.D. degree in theoretical and applied mechanics from Sapienza Università di Roma. During the Ph.D. study, he was a Visiting Student Research Collaborator with the Complex Fluids Group, Princeton University. After the Ph.D. study, he was first a Postdoctoral Researcher with the International School for Advanced Studies (SISSA), Trieste, Italy, then an Assistant Professor with The BioRobotics Institute, Scuola Superiore Sant'Anna, Pisa, Italy, where he was later promoted to an Associate Professor. He is currently an Associate Professor with the Department of Mechanical and Production Engineering, Aarhus University, where he leads the Computational Physics and Machine Learning Laboratory. His main research interests include the theoretical and computational modeling of multi-physics systems, including polymer-based smart materials, biological tissues, and soft robots, and also using novel approaches with the intersection between mechanics, (discrete) differential geometry, and machine learning. In 2022, he was awarded the ERC Starting Grant with the project "AI-based Learning for Physical Simulation (ALPS)," where he will develop new algorithms for the mathematical modeling of physical systems starting from experimental data.

● ● ●